An Accurate Sparse SAR Imaging Method for Enhancing Region-Based Features Via Nonconvex and TV Regularization

Zhongqiu Xu , Mingqian Liu , Guoru Zhou, Zhonghao Wei , Bingchen Zhang, and Yirong Wu

Abstract—With the rapid development of compressed sensing theories and applications, sparse signal processing has been widely used in synthetic aperture radar (SAR) imaging during the recent years. As an efficient tool for sparse reconstruction, ℓ_1 optimization induces sparsity the most effectively, and the ℓ_1-norm penalty is usually combined with the total variation norm (TV-norm) penalty to construct a compound regularizer in order to enhance the point-based features as well as the region-based features. However, as a convex optimizer, the analytic solution of ℓ_1 regularization-based sparse signal reconstruction is usually a biased estimation. Aiming at this issue, in this article, we quantitatively analyzed the variation of reconstruction bias with respect to the complex reflectivity of targets, the undersampling ratio and the noise power. In order to reduce the bias effect and improve the reconstruction accuracy, we adopted the nonconvex regularization-based sparse SAR imaging method with a nonconvex penalty family. Furthermore, we linearly combined the nonconvex penalty and the TV-norm penalty to form a compound regularizer in the imaging model, which can improve the reconstruction accuracy of distributed targets and maintain the continuity of the backscattering coefficient. Simulation results showed that compared with ℓ_1 regularization, nonconvex regularization can reduce the average relative bias from 10.88% to 0.25%; compared with the matched filtering method and ℓ_1 and TV regularization, nonconvex & TV regularization can reduce the variance of the uniformly distributed targets by 80% without losing of reconstruction accuracy. Experiments on Gaofen-3 SAR data are also exploited to verify the effectiveness of the proposed method.

Index Terms—Bias effect, nonconvex regularization, sparse SAR imaging, synthetic aperture radar (SAR), total variation (TV) regularization.

I. INTRODUCTION

S YNTHETIC aperture radar (SAR) is an active remote sensing technology, which carries on a moving platform, transmits electromagnetic wave to the scene, receives radar echo, and generates high-resolution microwave images via signal processing. Due to the radar resolving theory and Nyquist–Shannon sampling theorem, improvement of SAR system performance usually comes with the remarkably increased sampling data amount, and brings complexities to the system design and implementation [1]. In recent years, sparse signal processing is widely used in SAR imaging with the development of compressed sensing and related theories, which shows that a sparse signal can be effectively reconstructed with much fewer samples than that required by Nyquist–Shannon sampling theorem [2],[3]. In addition, for full sampling systems, sparse signal processing is also beneficial in terms of improving reconstruction performance. Sparse microwave imaging works effectively in multiple SAR modes, including stripmap SAR, ScanSAR, spotlight SAR, and TOPS SAR [4]–[6].

As an efficient tool for sparse reconstruction, ℓ_1 optimization is the most effective method in terms of enforcing the sparsity constraint. When adopted in SAR imaging, it can even suppress the sidelobes and reduce the imaging noise level. Using the ℓ_1 constraint, ℓ_1 optimization is often implemented via regularization and can be solved via several algorithms such as iterative shrinkage and thresholding algorithm (ISTA), alternating direction method of multipliers (ADMM) [7], and complex approximate message passing (CAMP) [8]. Point-based features in SAR images can be enhanced via ℓ_1 regularization due to its ability of reconstructing with good energy concentration. On the other hand, region-based features are also important for many applications such as target classification and image segmentation. As such, total variation norm (TV-norm) constraint of the image magnitude is introduced into the SAR imaging model in order to preserve the piecewise-constant features, which means that, the TV-norm constraint is capable of maintaining the continuity of the backscattering coefficients (σ_0) of distributed targets within a certain scene area [9], [10]. In real applications, we need to enhance both point-based features and region-based features, and as a result, we will linearly combine ℓ_1-norm penalty and the TV-norm penalty to construct a compound regularizer [11]–[13].

However, the ℓ_1-norm penalty is convex, and the analytic solution of the ℓ_1 regularization-based sparse signal reconstruction algorithm is usually a biased estimation [14], [15]. Such issue leads to the underestimation of targets' reflectivity when applied to sparse SAR imaging and results in bias effect of reconstruction, which finally affects the reconstruction accuracy [16], [17].

In this article, we define absolute and relative biases for quantitative analysis. Studies show that the bias effect is affected by these three factors [16]: amplitude of targets' complex reflectivity, undersampling ratio, and noise power. Among the above three factors, complex reflectivity of targets and undersampling ratio affect the signal energy, and noise power affects the noise energy. First, the relationship between ℓ_1 regularization reconstruction results and the ground truth is nonlinear, and the bias effect of the weak targets is more obvious than that of the strong targets. Second, the bias increases significantly as the sampling ratio decreases. Finally, as the noise power decreases, the quality of SAR imaging deteriorates, and the bias effect becomes more apparent. Therefore, estimation bias would have negative effects on the SAR image applications, such as target detection and radar cross section (RCS) estimation.

In order to promote more sparsity amid reducing the bias effect, this article focuses on nonconvex optimization. Popular examples of nonconvex optimization include the minimax concave (MC) penalty [17]–[19], smoothly clipped absolute deviation (SCAD) [20], log sum penalty (LSP), and ℓ_q-norm penalty (where $0 < q < 1$) [21]. The geometric and optimization properties of nonconvex penalties are more similar to that of ℓ_0-norm penalty compared with ℓ_1-norm penalty. Therefore, the nonconvex optimization algorithms are considered to be capable of improving the reconstruction accuracy and suppressing the bias effect. A commonly used approach of solving the nonconvex optimization is the multi-stage convex relaxation or the so-called difference of convex functions programming [22], which is hardly used in large-scale problems due to its high computational cost. Recent works have shown that some proximal methods can be utilized to solve the nonconvex optimizations when a simple closed-form solution of the proximal operators (with respect to the specific nonconvex optimization) can be derived [23]. Typical ones include the general iterative shrinkage-thresholding algorithm (GIST) and the proximal gradient-based ADMM [21], [23]. In this article, we choose the GIST algorithm for its succinctness and effectiveness. Also, recall that TV-norm optimization can enhance the region-based features [9], [10]; therefore, here we linearly combine the nonconvex penalty and the TV-norm penalty to form a compound regularizer in the imaging model, which can improve the reconstruction accuracy of distributed targets as well as maintain the continuity of the backscattering coefficients. For solving the compound regularization, this article adopts the variable splitting method, supplemented by alternating minimization method [24].

In large-scale SAR imaging problems, the measurement matrix is usually very huge. The storage and processing of such a matrix could be very costly, and even intractable. Therefore, we adopt the azimuth-range decouple scheme to the real data processing, in which azimuth-range decouple operators are implemented to substitute the measurement matrix and its Hermitian transpose to accelerate the signal processing and reduce the data amount [4].

In this article, we present an accurate SAR imaging algorithm by combining the aforementioned nonconvex regularization, TV-norm regularization, and azimuth-range decouple scheme. The proposed method can reduce the bias effect, maintain the continuity of distributed targets, and avoid the huge spatial/temporal complexities in computation. Experiments on real data of Gaofen-3 spaceborne SAR are also exploited to verify the effectiveness of the proposed method.

The remainder of this article is organized as follows. Section II introduces the sparse SAR imaging model, analyzes the bias effect of ℓ_1 regularization, and proposes an accurate and feature enhanced sparse SAR imaging method based on nonconvex & TV regularization. Simulation and experiment results are given in Section III. Discussions related to the variation of bias effect with respect to the undersampling ratios and noise power, and quantitative analysis of reconstruction continuity are provided in Section IV. Section V summarizes the contribution of this article.

II. SPARSE SAR IMAGING BASED ON NONCONVEX & TV REGULARIZATION

A. Sparse SAR Imaging Formation

The relationship between the SAR measurements and the reflectivity of the scene is expressed as [1]

$$\boldsymbol{y} = \boldsymbol{\Phi}\boldsymbol{\alpha} + \boldsymbol{n} \qquad (1)$$

where $\boldsymbol{y} \in \mathbb{C}^{M \times 1}$ is the vector form of the echo data, $\boldsymbol{\alpha} \in \mathbb{C}^{N \times 1}$ is the vector form of the SAR image, and $\boldsymbol{n} \in \mathbb{C}^{M \times 1}$ is the additive noise. $\boldsymbol{\Phi} \in C^{M \times N}$ is the corresponding measurement matrix of the imaging system which links the measurements $\boldsymbol{y}$ and the target scene $\boldsymbol{\alpha}$.

The SAR imaging process can be considered as a linear inverse problem (LIP), in which we try to solve $\boldsymbol{\alpha}$ from $\boldsymbol{y}$ and $\boldsymbol{\Phi}$. The most commonly used method for solving LIPs is to minimize the regularized linear least squares (LS) cost function

$$\min_{\boldsymbol{\alpha}} \|\boldsymbol{y} - \boldsymbol{\Phi}\boldsymbol{\alpha}\|_2^2 + \lambda p(\boldsymbol{\alpha}) \qquad (2)$$

where $p(\cdot)$ is the constraint and we implemented it in the cost function as a penalty term or *regularizer*, and λ is the regularization parameter.

In order to promote sparsity in $\boldsymbol{\alpha}$, we need a regularization term that increases when the number of active components grows. The obvious choice is to use the ℓ_0-norm that returns directly the number of nonzero coefficients in $\boldsymbol{\alpha}$. However, ℓ_0 regularization is a nondeterministic polynomial-time hard (NP-hard) problem; therefore, we need to relax the penalty function to make it mathematical solvable. According to [25], for k-sparse signal, if the measurement matrix $\boldsymbol{\Phi}$ satisfies $\delta_{2k} < \sqrt{2} - 1$ where δ_{2k} is the $2k$-order restricted isometry constant of $\boldsymbol{\Phi}$, the solution of the ℓ_1 problem is guaranteed to match that of the ℓ_0 problem. In other words, the convex relaxation is exact. The relaxed ℓ_1 regularization-based SAR imaging model is formulated as

$$min_{\boldsymbol{\alpha}} \|\boldsymbol{y} - \boldsymbol{\Phi}\boldsymbol{\alpha}\|_2^2 + \lambda \|\boldsymbol{\alpha}\|_1 \qquad (3)$$

where

$$\|\boldsymbol{\alpha}\|_1 = \sum_{i=1}^{N} (|\alpha_i|) \qquad (4)$$

with α_i as the ith element of $\boldsymbol{\alpha}$.

Sparsity-inducing regularizers are aimed at enhancing point-based features of SAR images, while region-based features are also important for many applications such as target classification and image segmentation. We are thus interested in maintaining the continuity of the backscattering coefficient (σ_0) of distributed targets within a certain area, which can be implemented via the TV-norm [9], [10]. For 2-D scenes, the discrete isotropic TV-norm of image vector $\boldsymbol{\alpha}$ is defined as follows:

$$TV(|\boldsymbol{\alpha}|) = \sum_{i,j} \left\| \nabla(|\boldsymbol{A}|_{i,j}) \right\|_2 \qquad (5)$$

where $\boldsymbol{A}$ is the 2-D complex-valued matrix corresponding to image vector $\boldsymbol{\alpha}$, the operator $|\cdot|$ represents element-wise magnitude calculation, and $\nabla(|\boldsymbol{A}|_{i,j})$ is the gradient vector of pixel in the ith row and jth column, which is defined as

$$\nabla(|\boldsymbol{A}|_{i,j}) = (D_h |\boldsymbol{A}|_{i,j}, D_v |\boldsymbol{A}|_{i,j}) \qquad (6)$$

with

$$D_h |\boldsymbol{A}|_{i,j} = |\boldsymbol{A}[i+1,j]| - |\boldsymbol{A}[i,j]| \qquad (7)$$

$$D_v |\boldsymbol{A}|_{i,j} = |\boldsymbol{A}[i,j+1]| - |\boldsymbol{A}[i,j]|. \qquad (8)$$

Combining ℓ_1-norm penalty and the TV-norm penalty linearly to form a compound regularizer, then the optimization problem (3) becomes

$$\min_{\boldsymbol{\alpha}} \|\boldsymbol{y} - \boldsymbol{\Phi}\boldsymbol{\alpha}\|_2^2 + \lambda_1 \|\boldsymbol{\alpha}\|_1 + \lambda_2 TV(|\boldsymbol{\alpha}|). \qquad (9)$$

This expression is expected to enhance both point-based features and region-based features of SAR images.

B. Analysis of Bias Effect Caused by ℓ_1 Regularization

The ℓ_1 regularization-based SAR imaging model is described in formula (3). However, ℓ_1 regularization is known as a biased estimator. Suppose $\boldsymbol{\alpha}^{\ell_1}$ is the result of ℓ_1 regularization and S is its support set. The reference shows that for the nonzero part of $\boldsymbol{\alpha}^{\ell_1}$, the estimation is formulated as [14], [15]

$$\begin{aligned} \boldsymbol{\alpha}_S^{\ell_1} &= (\boldsymbol{\Phi}_S^H \boldsymbol{\Phi}_S)^{-1} \boldsymbol{\Phi}_S^H \boldsymbol{s} - \lambda (\boldsymbol{\Phi}_S^H \boldsymbol{\Phi}_S)^{-1} sign(\boldsymbol{\alpha}_S^{\ell_1}) \\ &= (\boldsymbol{\Phi}_S^H \boldsymbol{\Phi}_S)^{-1} (\boldsymbol{\Phi}_S^H \boldsymbol{s} - \lambda sign(\boldsymbol{\alpha}_S^{\ell_1})) \end{aligned} \qquad (10)$$

where $\boldsymbol{\Phi}_S$ is the column submatrix of $\boldsymbol{\Phi}$ supported on S and $\boldsymbol{\alpha}_S^{\ell_1}$ is the subvector on S, and $(\cdot)^H$ denotes the Hermitian transpose. The first part of (10), $(\boldsymbol{\Phi}_S^H \boldsymbol{\Phi}_S)^{-1} \boldsymbol{\Phi}_S^H \boldsymbol{s}$, is the LS estimation, which is the unbiased estimation, and the second part, $\lambda (\boldsymbol{\Phi}_S^H \boldsymbol{\Phi}_S)^{-1}$, is the bias. Therefore, as described in (10), the solution of (3) based on ℓ_1 regularization is the biased estimation according to statistical signal processing.

The bias effect that was analyzed above shows a significant effect on the reconstruction accuracy when applied to sparse SAR imaging. In order to quantitatively analyze the bias effect, we define two evaluation criteria: absolute bias (AB) and relative bias (RB) as follows [16], [26]:

$$AB(\sigma_i) = |\hat{\sigma}_i - \sigma|, \; AB(\boldsymbol{\sigma}) = \frac{1}{N} \sum_{i=1}^{N} AB(\sigma_i), \qquad (11)$$

$$RB(\sigma_i) = \frac{|\hat{\sigma}_i - \sigma|}{|\sigma|}, \; RB(\boldsymbol{\sigma}) = \frac{1}{N} \sum_{i=1}^{N} RB(\sigma_i), \qquad (12)$$

where $\boldsymbol{\sigma}$ is the the vector form of the SAR image and $\hat{\boldsymbol{\sigma}}$ is the estimation of $\boldsymbol{\sigma}$ based on ℓ_1 regularization. ℓ_1 regularization can be solved via ISTA [8]. Considering the properties of ISTA, when a system is determined, the noise level and the threshold function are two factors which influence the bias of the result. So we analyze the influence of complex reflectivity on the bias effect from the perspective of the threshold function. According to Elad [8], the threshold function corresponding to ℓ_1 regularization is the soft thresholding function soft$() : \mathbb{R} \to \mathbb{R}$

$$soft(\alpha_i; \lambda) = \begin{cases} 0, & |\alpha_i| \le \lambda \\ (|\alpha_i| - \lambda) sign(\alpha_i), & |\alpha_i| \ge \lambda \end{cases}. \qquad (13)$$

The absolute bias and relative bias between input and output of soft$(\alpha_i; \lambda)$ can be calculated as follows:

$$\begin{aligned} AB_{soft}(\alpha_i) &= \begin{cases} |\alpha_i|, & |\alpha_i| \le \lambda \\ \lambda, & |\alpha_i| \ge \lambda \end{cases} \\ RB_{soft}(\alpha_i) &= \begin{cases} 1, & |\alpha_i| \le \lambda \\ \dfrac{\lambda}{|\alpha_i|}, & |\alpha_i| \ge \lambda \end{cases} \end{aligned} \qquad (14)$$

As shown in Fig. 1, the relative bias of $soft(\alpha_i, \lambda)$ increases as the magnitude of α_i decreases, which means that in sparse SAR imaging based on ℓ_1 regularization, the bias effect has a greater impact on targets with lower reflectivity.

C. Nonconvex & TV Regularization

ℓ_1-Norm penalty is convex and the analytical solution of the ℓ_1 regularization-based sparse signal reconstruction algorithm is a biased estimation. In order to promote more sparsity while reducing the bias, several works have looked at nonconvex but continuous regularization [27]. Popular examples include the SCAD penalty [20], MC penalty [18], [19], LSP, and ℓ_q-norm penalty with $0 < q < 1$ [21]. The scalar mathematical expressions of these commonly used nonconvex penalties are given in the second column of Table I. We plot curves of ℓ_0-norm penalty, ℓ_1-norm penalty, and typical nonconvex penalties listed in Table I when $\boldsymbol{\alpha}$ is a 1×1 vector, as shown in Fig. 2. It can be seen that the geometrical properties of nonconvex penalties are more similar to that of ℓ_0-norm penalty compared with ℓ_1-norm penalty. As a result, nonconvex regularization can promote more sparsity while reducing the bias. Therefore, we propose to utilize these advantages of nonconvex penalties to suppress bias effect and achieve accurate reconstruction. The nonconvex regularization-based SAR imaging model is formulated as

$$\min_{\boldsymbol{\alpha}} \|\boldsymbol{y} - \boldsymbol{\Phi}\boldsymbol{\alpha}\|_2^2 + \lambda p_{NC}(\boldsymbol{\alpha}) \qquad (15)$$

where $p_{NC}(\cdot)$ represents the nonconvex penalty. In the above four nonconvex penalties, the 1-D curves of the SCAD penalty and the MC penalty are closer to ℓ_0-norm penalty compared with the LSP penalty and the ℓ_q-norm penalty, which means that the reconstruction performance of SCAD or MC is more approximate to ℓ_0 regularization.

TABLE I
SCALAR EXPRESSIONS OF COMMONLY USED NONCONVEX PENALTIES WITH THEIR THRESHOLDING FUNCTIONS

Penalty name	Penalty formulation	Thresholding function
$\alpha_i = argmin_{\alpha_i} \dfrac{L}{2}(\alpha_i - z_i)^2 + \lambda p(\alpha_i)$ $= argmin_{\alpha_i} \dfrac{1}{2}(\alpha_i - z_i)^2 + \lambda p(\alpha_i) = threshold(z_i, \lambda), \ \lambda = \dfrac{\lambda}{L}$		
L_q-norm penalty $(0 < q < 1)$	$\lambda p_{L_q}(\alpha_i) = \lambda \left|\alpha_i\right|^q$	$threshold_{L_q}(z_i, \lambda) =$ $\begin{cases} 0, & \left|z_i\right| < \tau \\ \{0, sign(z_i)\beta\}, & \left|z_i\right| = \tau \\ sign(z_i)y, & \left|z_i\right| > \tau \end{cases}$ $\beta = [2\lambda(1-q)]^{1/(2-q)}, \tau = \beta + \lambda q \beta^{q-1}$ $h(y) = \lambda q y^{q-1} + y - \left|\alpha_i\right| = 0, y \in [\beta, \left|z_i\right|]$
Log sum penalty $(\theta > 0)$	$\lambda p_{LSP}(\alpha_i) = \lambda log(1 + \left|\alpha_i\right|/\theta)$	$threshold_{LSP}(z_i, \lambda) = sign(z_i)x$ $where \ x =$ $argmin_{\alpha_i} \dfrac{L}{2}(\alpha_i - \left|z_i\right|)^2 + \lambda log(1 + \alpha_i/\theta)$ $s.t. \ \alpha_i \geq 0$
MC penalty $(\theta > 1)$	$\lambda p_{MC}(\alpha_i) =$ $\begin{cases} \lambda(\left|\alpha_i\right| - \dfrac{\alpha_i^2}{2\theta}), & \left|\alpha_i\right| \leq \theta \\ \lambda\theta/2, & \left|\alpha_i\right| > \theta \end{cases}$	$threshold_{MC}(z_i, \lambda) =$ $\begin{cases} 0, & \left|z_i\right| < \lambda \\ \theta\lambda \dfrac{\left|z_i\right| - \lambda}{\theta\lambda - \lambda} sign(z_i), & \lambda \leq \left|z_i\right| \leq \theta\lambda \\ z_i, & \left|z_i\right| > \theta\lambda \end{cases}$
SCAD penalty $(\theta > 2)$	$\lambda p_{SCAD}(\alpha_i) =$ $\begin{cases} \lambda \left|\alpha_i\right|, & \left|\alpha_i\right| \leq \lambda \\ \dfrac{-\alpha_i^2 + 2\theta\lambda\left|\alpha_i\right| - \lambda^2}{2(\theta-1)}, & \lambda < \left|\alpha_i\right| \leq \theta\lambda \\ (\theta+1)\lambda^2/2, & \left|\alpha_i\right| > \theta\lambda \end{cases}$	$threshold_{SCAD}(z_i, \lambda) =$ $\begin{cases} sign(z_i)(\left|z_i\right| - \lambda), & \left|z_i\right| < \lambda \\ \dfrac{(\theta-1)z_i - sign(z_i)\theta\lambda}{\theta-2}, & \lambda \leq \left|z_i\right| \leq \theta\lambda \\ z_i, & \left|z_i\right| > \theta\lambda \end{cases}$

For Image Vector $\boldsymbol{\alpha}$, the Penalty Function is the Sum of the Scalar Expressions Corresponding to Each Element: $\lambda p(\boldsymbol{\alpha}) = \lambda \sum_{i=1}^{N} p(\alpha_i)$.

When we focus on region-based features of the SAR image, it is necessary to add TV-norm as a constraint in the model considering that TV-norm optimization will emphasize more on piecewise-constant features. Therefore, we linearly combine the nonconvex penalty and the TV-norm penalty to construct a compound regularizer, generating a new sparse SAR imaging model as follows:

$$\min_{\boldsymbol{\alpha}} \left\|\boldsymbol{y} - \boldsymbol{\Phi}\boldsymbol{\alpha}\right\|_2^2 + \lambda_1 p_{NC}(\boldsymbol{\alpha}) + \lambda_2 TV(\left|\boldsymbol{\alpha}\right|) \quad (16)$$

which is expected to improve the reconstruction accuracy and maintain the continuity of the backscattering coefficient (σ_0) of distributed targets within a certain area in the same time.

D. Reconstruction Algorithms

1) LIPs With Nonconvex Penalties—Optimization Problem (15): For convenience, we use $f(\boldsymbol{\alpha})$ to represent $\left\|\boldsymbol{y} - \boldsymbol{\Phi}\boldsymbol{\alpha}\right\|_2^2$, then we consider solving the following optimization problem

$$\min_{\boldsymbol{\alpha}} f(\boldsymbol{\alpha}) + \lambda p_{NC}(\boldsymbol{\alpha}). \quad (17)$$

According to the idea of GIST algorithm [23], we perform a second-order Taylor expansion on $f(\boldsymbol{\alpha})$ at point $\boldsymbol{\alpha}^k$. When $\nabla f(\boldsymbol{\alpha}^k)$ satisfies L-Lipschitz continuous condition, $f(\boldsymbol{\alpha})$ can be approximated into the following form:

$$f(\boldsymbol{\alpha}) = \frac{L}{2}\left\|\boldsymbol{\alpha} - (\boldsymbol{\alpha}^k - \frac{1}{L}\nabla f(\boldsymbol{\alpha}^k))\right\|_2^2 + C(\boldsymbol{\alpha}^k) \quad (18)$$

where $C(\boldsymbol{\alpha}^k)$ is a constant term that does not depend on $\boldsymbol{\alpha}$. Therefore, the optimization problem (15) can be solved by generating a sequence $\{\boldsymbol{\alpha}^k\}$ via

$$\boldsymbol{\alpha}^{k+1} =$$

$$argmin_{\boldsymbol{\alpha}} \frac{L}{2}\left\|\boldsymbol{\alpha} - (\boldsymbol{\alpha}^k - \frac{1}{L}\nabla f(\boldsymbol{\alpha}^k))\right\|_2^2 + \lambda p_{NC}(\boldsymbol{\alpha}) =$$

$$argmin_{\boldsymbol{\alpha}} \frac{L}{2}\left\|\boldsymbol{\alpha} - (\boldsymbol{\alpha}^k + \frac{1}{L}\boldsymbol{\Phi}^H(y - \boldsymbol{\Phi}\boldsymbol{\alpha}^k))\right\|_2^2 + \lambda p_{NC}(\boldsymbol{\alpha}).$$

$$(19)$$
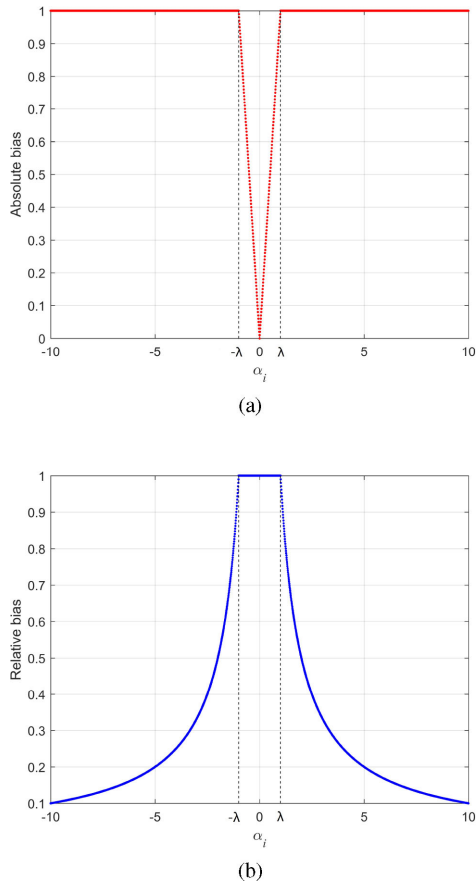
Fig. 1.   The absolute bias and relative bias of $soft(\alpha_i; \lambda)$ supposing $\lambda = 1$. (a) $AB_{soft}(\alpha_i)$. (b) $RB_{soft}(\alpha_i)$.
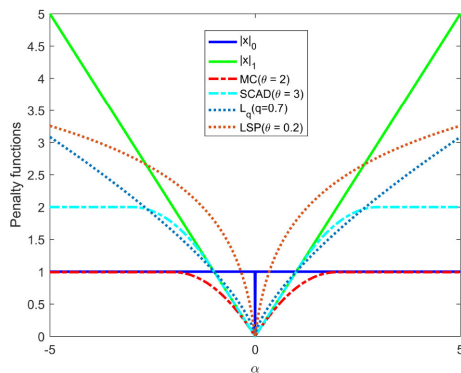

Fig. 2.   Curves of ℓ_0-norm penalty, ℓ_1-norm penalty, and typical nonconvex penalties listed in Table I when $\boldsymbol{\alpha}$ is a 1×1 vector.

Observing the first term to the right of the equal sign in (19), it is obvious that

$$z^{k+1} = \alpha^k - \frac{1}{L}\nabla f(\alpha^k) = \alpha^k + \frac{1}{L}\Phi^H(y - \Phi\alpha^k) \quad (20)$$

is the optimal solution of $argmin_\alpha f(\alpha)$ according to the principle of gradient descent. Then, problem (15) is equivalent to

the following proximal operator problem:

$$\boldsymbol{\alpha}^{k+1} = argmin_\alpha \frac{L}{2} \left\| \boldsymbol{\alpha} - \boldsymbol{z}^{k+1} \right\|_2^2 + \lambda p_{NC}(\boldsymbol{\alpha}). \quad (21)$$

Therefore, in GIST, we first perform a gradient descent along the direction $-\nabla f(\boldsymbol{\alpha^k})$ with step size $1/L$ and then solve a proximal operator problem. According to [23], there exists a simple closed-form solution to the proximal operator problem in (21) if the penalty function $p_{NC}(\boldsymbol{\alpha})$ satisfies the following three assumptions.

- $p_{NC}(\boldsymbol{\alpha})$ is a continuous function which is possibly nonsmooth and nonconvex, and can be rewritten as the difference of two convex functions.
- $p_{NC}(\boldsymbol{\alpha})$ can be written as $\lambda p_{NC}(\boldsymbol{\alpha}) = \lambda \sum_{i=1}^{N} p_{NC}(\alpha_i)$.
- The objective function is lower bounded.

The objective function in (21) can be written as the sum of multiple subproblems

$$\sum_{i=1}^{N} \left[\frac{L}{2}(\alpha_i - z_i^{k+1})^2 + \lambda p_{NC}(\alpha_i) \right] \quad (22)$$

then, the original problem can be solved by optimizing these N subproblems. It can be easily verified that the four nonconvex penalties mentioned in Section II-C all satisfy the above conditions, so their proximal operators have closed-form solutions and they are usually named as *thresholding functions*, as given in the third column of Table I.

2) LIPs With Nonconvex and TV-Norm Penalties— Optimization Problem (16): Under the guidance of variable splitting methods [24], [28], [29], we convert unconstrained problem (16) into the following equivalent constrained optimization problem:

$$\min_{\boldsymbol{\alpha}, \boldsymbol{z_1}, \boldsymbol{z_2}} \|\boldsymbol{y} - \boldsymbol{\Phi}\boldsymbol{\alpha}\|_2^2 + \lambda_1 p_{NC}(\boldsymbol{z_1}) + \lambda_2 TV(|\boldsymbol{z_2}|)$$
$$(23)$$
$$\text{subject to } \|\boldsymbol{\alpha} - \boldsymbol{z_1}\|_2^2 = 0, \|\boldsymbol{\alpha} - \boldsymbol{z_2}\|_2^2 = 0$$

where $\boldsymbol{z_1}, \boldsymbol{z_2}$ are two auxiliary variables. According to the principle of Lagrangian multiplier method, the above optimization problem can be solved via minimizing the following formula:

$$L(\boldsymbol{\alpha}, \boldsymbol{z_1}, \boldsymbol{z_2}, l_1, l_2) = \|\boldsymbol{y} - \boldsymbol{\Phi}\boldsymbol{\alpha}\|_2^2 + \lambda_1 p_{NC}(\boldsymbol{z_1})$$
$$+ \lambda_2 TV(|\boldsymbol{z_2}|) + l_1 \|\boldsymbol{\alpha} - \boldsymbol{z_1}\|_2^2 + l_2 \|\boldsymbol{\alpha} - \boldsymbol{z_2}\|_2^2 \quad (24)$$

with l_1 and l_2 as Lagrange multipliers. Correspondingly, the optimal solution should have the following expression:

$$(\boldsymbol{\alpha}^*, \boldsymbol{z_1}^*, \boldsymbol{z_2}^*) = argmin_{\boldsymbol{\alpha}, \boldsymbol{z_1}, \boldsymbol{z_2}} L(\boldsymbol{\alpha}, \boldsymbol{z_1}, \boldsymbol{z_2}, l_1, l_2). \quad (25)$$

To minimize $L(\boldsymbol{\alpha}, \boldsymbol{z_1}, \boldsymbol{z_2}, l_1, l_2)$, we propose to use the alternating minimization method with respect to variables $\boldsymbol{\alpha}, \boldsymbol{z_1}, \boldsymbol{z_2}$, while gradually increasing the values of the Lagrange multipliers l_1, l_2 with iteration [24], and the iterative procedure is as follows:

$$\boldsymbol{\alpha}^{(t+1)} = argmin_\alpha \|\boldsymbol{y} - \boldsymbol{\Phi}\boldsymbol{\alpha}\|_2^2 + \sum_{i=1}^{2} l_i \left\| \boldsymbol{\alpha} - \boldsymbol{z_i}^{(t)} \right\|_2^2$$
$$(26)$$

$$\boldsymbol{z_1}^{(t+1)} = argmin_{\boldsymbol{z_1}} l_1 \left\| \boldsymbol{z_1} - \boldsymbol{\alpha}^{(t+1)} \right\|_2^2 + \lambda_1 p_{NC}(\boldsymbol{z_1})$$
$$(27)$$

$$z_{\mathbf{2}}^{(t+1)} = argmin_{z_{\mathbf{2}}} \, l_2 \left\| z_{\mathbf{2}} - \boldsymbol{\alpha}^{(t+1)} \right\|_2^2 + \lambda_2 TV(|z_{\mathbf{2}}|). \tag{28}$$

The minimization in (26), since the objective function is quadratic, yields a linear system of equations with solution

$$\boldsymbol{\alpha}^{(t+1)}$$
$$= \left[\boldsymbol{\Phi}^{\boldsymbol{H}} \boldsymbol{\Phi} + (l_1 + l_2) \boldsymbol{I} \right]^{-1} \left[\boldsymbol{\Phi}^{\boldsymbol{H}} \boldsymbol{y} + l_1 z_{\mathbf{1}}^{(t)} + l_2 z_{\mathbf{2}}^{(t)} \right]. \tag{29}$$

The optimization problem in (27) is the same as (21) in Section II-D.1, which belongs to the proximal operator problem, and there exists a simple closed-form solution to it if the penalty function $p_{NC}(\boldsymbol{\alpha})$ satisfies some specific conditions. Therefore, problem (27) has the optimal solution as follows:

$$z_{\mathbf{1}}^{(t+1)} = threshold_{NC}(\boldsymbol{\alpha}^{(t+1)}, \lambda_{NC}) \\ \text{with } \lambda_{NC} = \lambda_1/(2l_1) \tag{30}$$

where $threshold_{NC}$ represents the thresholding function corresponding to the nonconvex penalty as shown in Table I.

For TV regularization shown in (28), we borrow the Chambolle algorithm [9], which obtains the solution by solving the dual problem of TV regularization. After parameter transformation, (28) is equivalent to the following standard TV regularization problem:

$$z_{\mathbf{2}}^{(t+1)} = argmin_{z_{\mathbf{2}}} \, \frac{1}{2} \left\| z_{\mathbf{2}} - \boldsymbol{\alpha}^{(t+1)} \right\|_2^2 + \lambda_{TV} TV(|z_{\mathbf{2}}|) \\ \text{with } \lambda_{TV} = \lambda_2/(2l_2). \tag{31}$$

The solution to the above optimization problem is

$$z_{\mathbf{2}}^{(t+1)} = sign(\boldsymbol{\alpha}^{(t+1)})(\left| \boldsymbol{\alpha}^{(t+1)} \right| - \lambda_{TV} div(\boldsymbol{p}^{(t+1)})) \tag{32}$$

where $\boldsymbol{p} = (\boldsymbol{p}^1, \boldsymbol{p}^2) \in Y$ is the dual variable of $z_{\mathbf{2}} \in X$ and can be solved by the projected gradient descent method

$$p_{i,j}^{(t+1)} = \\ \frac{p_{i,j}^{(t)} + \tau(\nabla(div\boldsymbol{p}^{(t)} - \left| \boldsymbol{\alpha}^{(t+1)} \right| / \lambda_{TV}))_{i,j}}{\max \left\{ 1, \left| p_{i,j}^{(t)} + \tau(\nabla(div\boldsymbol{p}^{(t)} - \left| \boldsymbol{\alpha}^{(t+1)} \right| / \lambda_{TV}))_{i,j} \right| \right\}}. \tag{33}$$

Symbol $div = -\nabla^*$ is the discrete divergence operator ($div : Y \to X, \nabla : X \to Y$)

$$(div\boldsymbol{p})_{i,j} = \begin{cases} p_{i,j}^1 - p_{i-1,j}^1, & 1 < i < N \\ p_{i,j}^1, & i = 1 \\ -p_{i-1,j}^1, & i = N \end{cases} \\ + \begin{cases} p_{i,j}^2 - p_{i,j-1}^2, & 1 < i < N \\ p_{i,j}^2, & i = 1 \\ -p_{i,j-1}^2, & i = N \end{cases}. \tag{34}$$

In (33), τ represents the iteration step size, which needs to meet the following condition: $0 < \tau < 1/4$, and we generally take τ equal to the constant 0.248 [10].

3) Azimuth-Range Decouple Scheme: As described in Sections II-D.1 and II-D.2, the nonconvex regularization-based SAR imaging method and the nonconvex & TV regularization-based SAR imaging method all have to store and process the large-scale measurement matrix, which would bring huge memory and computational cost. Thus, we adopt the azimuth-range decouple scheme in the real data processing [4]. Azimuth-range decouple operators can be implemented to substitute the measurement matrix and its Hermitian transpose. Supposing that $G(\cdot)$ is the raw data generation operator and $I(\cdot)$ is the imaging operator (their detailed expression can be found in [4]), the azimuth-range decouple scheme is formulated as

$$\boldsymbol{\Phi}\boldsymbol{\alpha} \cong G(\boldsymbol{\alpha}), \; \boldsymbol{\Phi}^H \boldsymbol{y} \cong I(\boldsymbol{y}). \tag{35}$$

Applying these two operators to iterations, the two algorithms described in Sections II-D.1 and II-D.2 are replaced by the azimuth-range decouple versions, which can avoid the huge memory and computational costs, as shown in Figs. 3 and 4. Azimuth-range decouple operators can directly process the 2-D echo data; therefore, $\boldsymbol{\alpha}$ in the above algorithm represents the raw SAR image that is not vectorized. And $\| \cdot \|_2$ is defined as $\|\boldsymbol{\alpha}\|_2 = \sqrt{\sum_{i,j} \alpha_{i,j}^2}$.

Suppose that there are N_a points in the direction of azimuth and N_r points in the direction of range for the raw echo data, $N = N_a \times N_r$, the computational complexity of the matched filtering method can be expressed as $O(Nlog(N))$. When the number of iterations is I, the computational complexity of the measurement matrix-based sparse SAR imaging method will reach $O(IN^2)$, while the computational complexity of the azimuth-range decouple-based sparse SAR imaging method is only $O(INlog(N))$. Therefore, the speedup ratio of the azimuth-range decouple-based sparse SAR imaging method is $r_C = O(N/log(N))$.

III. EXPERIMENTAL RESULTS

A. Simulations

The simulation experiment is divided into two parts. First, we construct a 1-D scene and reconstruct it using ℓ_1 regularization in order to observe the variation of bias with respect to targets' amplitude. Under the same experimental conditions, we reconstruct the scene with nonconvex regularization, and compare the result with that of ℓ_1 regularization to verify the effectiveness of the method. Then, we construct a 2-D scene and reconstruct it with the chirp scaling algorithm (CSA) as well as the azimuth-range decouple operator-based ℓ_1/nonconvex & TV regularizations. The experimental results are compared to verify the effectiveness of TV regularization in enhancing region-based features, and the ability of nonconvex regularization to improve the reconstruction accuracy of distributed targets.

In the 1-D model, there are 1000 points in azimuth direction. We place a target every 50 points, a total of 20 targets with different reflectivity in the scene. A 1000×1000 Gaussian orthogonal matrix is chosen as the measurement matrix. First, at $SNR = 20$dB and full sampling conditions, we reconstruct the scene with ℓ_1 and nonconvex regularization. For convenience,

---

Algorithm 1 Azimuth-range decouple based nonconvex regularization for SAR imaging

---

Input: The echo data y, initial solution $\boldsymbol{\alpha}^{(0)} = \mathbf{0}$, the azimuth-range decouple operators $G(\cdot)$ and

$I(\cdot)$, error parameter ϵ, maximum number of iterations T_{max}, step size L, the number of nonzero

elements K, the component with the $(K+1)^{th}$ largest absolute value in the vector $|\cdot|_{K+1}$.

1: **while** $res > \epsilon$ and $t < T_{max}$ **do**

2:      $\Delta y^{(t)} = y - G(\boldsymbol{\alpha}^{(t)}), \Delta \boldsymbol{\alpha}^{(t)} = I(\Delta y^{(t)})$

3:      $z^{(t+1)} = \boldsymbol{\alpha}^{(t)} + \frac{1}{L}\Delta \boldsymbol{\alpha}^{(t)}, \lambda^{(t+1)} = L \left| z^{(t+1)} \right|_{K+1}$

4:      $\boldsymbol{\alpha}^{(t+1)} = argmin_{\boldsymbol{\alpha}} \frac{L}{2} \left\| \boldsymbol{\alpha} - z^{k+1} \right\|_2^2 + \lambda^{(t+1)} p(\boldsymbol{\alpha}) = threshold(z^{(t+1)}, \frac{\lambda^{(t+1)}}{L})$

5:      $res = \left\| \boldsymbol{\alpha}^{(t+1)} - \boldsymbol{\alpha}^{(t)} \right\|_2 / \left\| \boldsymbol{\alpha}^{(t)} \right\|_2$

6:      $t = t + 1$

7: **end while**

Output: $\hat{\boldsymbol{\alpha}} = \boldsymbol{\alpha}^{(t)}$

Fig. 3.   Azimuth-range decouple based nonconvex regularization for SAR imaging.

Algorithm 2 Azimuth-range decouple based nonconvex and TV regularization for SAR imaging

---

Input: The echo data y, initial solution $\boldsymbol{\alpha}^{(0)} = \mathbf{0}$, initial dual variable $\boldsymbol{p} = (\mathbf{0}, \mathbf{0})$, the azimuth-range

decouple operators $G(\cdot)$ and $I(\cdot)$, error parameter ϵ, maximum number of iterations T_{max}, step

size $\tau = 0.248$, image size N, variance of noise σ.

1: **while** $res > \epsilon$ and $t < T_{max}$ **do**

2:      $\boldsymbol{\alpha}^{(t+1)} = [I(G(\boldsymbol{I})) + (l_1 + l_2)\boldsymbol{I}]^{-1} \left[I(\boldsymbol{y}) + l_1 z_1^{(t)} + l_2 z_2^{(t)} \right]$

3:      $\lambda_1^{(t+1)} = 2l_1 (\left| \boldsymbol{\alpha}^{(t+1)} \right|_{K+1})$

4:      $z_1^{(t+1)} = argmin_{z_1} l_1 \left\| z_1 - \boldsymbol{\alpha}^{(t+1)} \right\|_2^2 + \lambda_1^{(t+1)} p(z_1) = threshold(\boldsymbol{\alpha}^{(t+1)}, \frac{\lambda_1^{(t+1)}}{2l_1})$

5:      $\lambda_2^{(t+1)} = \lambda_2^{(k)} \frac{N\sigma}{\left\| z_2^{(t)} - \boldsymbol{\alpha}^{(k+1)} \right\|_2}$

6:      $p_{i,j}^{(t+1)} = (p_{i,j}^1, p_{i,j}^2)^{(t+1)} = \frac{p_{i,j}^{(t)} + \tau(\nabla(div\boldsymbol{p}^{(t)} - \boldsymbol{\alpha}^{(t+1)}/\lambda_{TV}))_{i,j}}{max\left\{ 1, \left| p_{i,j}^{(t)} + \tau(\nabla(div\boldsymbol{p}^{(t)} - \boldsymbol{\alpha}^{(t+1)}/\lambda_{TV}))_{i,j} \right| \right\}}, \lambda_{TV}^{(t+1)} = \frac{\lambda_2^{(t+1)}}{2l_2}$

7:      $z_2^{(t+1)} = \boldsymbol{\alpha}^{(t+1)} - \lambda_{TV} div(\boldsymbol{p}^{(t+1)})$

8:      $res = \left\| \boldsymbol{\alpha}^{(t+1)} - \boldsymbol{\alpha}^{(t)} \right\|_2 / \left\| \boldsymbol{\alpha}^{(t)} \right\|_2$

9:      $t = t + 1$

10: **end while**

Output: $\hat{\boldsymbol{\alpha}} = \boldsymbol{\alpha}^{(t)}$

Fig. 4.   Azimuth-range decouple-based nonconvex and TV regularization for SAR imaging.
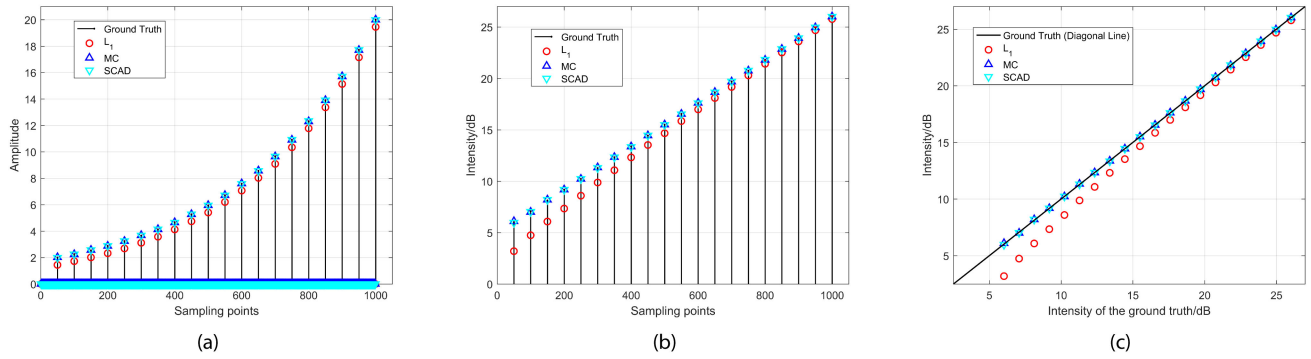
Fig. 5. Reconstruction results of targets with different reflectivity. (a) Amplitude image. (b) Intensity image with logarithmic scale. (c) The relative relationship with the ground truth.
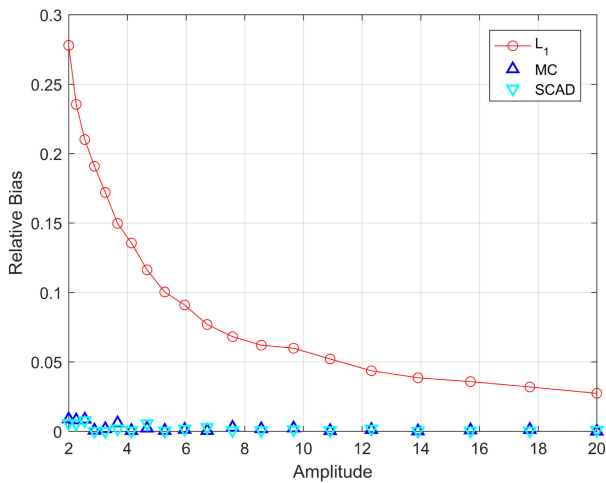

Fig. 6. Relative bias of targets with different reflectivity.

Fig. 7. Reconstruction results (amplitude) of the distributed target. (a) Chirp Scaling. (b) ℓ_1+TV. (c) MC+TV. (d) SCAD+TV.

we choose two typical nonconvex penalty functions: MC and SCAD rather than all examples listed in Table I. As shown in Fig. 5, the red circle indicates the result of ℓ_1 regularization, the blue upper triangle indicates the result of MC, and the cyan lower triangle indicates the result of SCAD. Obviously, ℓ_1 regularization underestimates the amplitude of the targets, while SCAD and MC can reconstruct the target more accurately. In Fig. 5(c), the ground truth is shown in the horizontal axis, and the figure shows the relative relationship between the reconstruction results of ℓ_1 regularization, nonconvex regularization, and the ground truth. It is obvious that the results of MC- and SCAD-based nonconvex regularization can preserve the linear relationship with the ground truth, while ℓ_1 regularization cannot. Therefore, the radiometric calibration using known external targets after the image reconstruction cannot eliminate the bias effect caused by ℓ_1 regularization. In order to quantitatively analyze the bias effect, we calculate the relative bias of results corresponding to these three sparse reconstruction algorithms, and the results are shown in Fig. 6. It can be seen that the relative bias of targets becomes larger as the amplitude of reflectivity decreases for ℓ_1 regularization, which means that the bias effect has a greater impact on weak targets. In contrast, nonconvex regularization can control the relative bias at a low level.
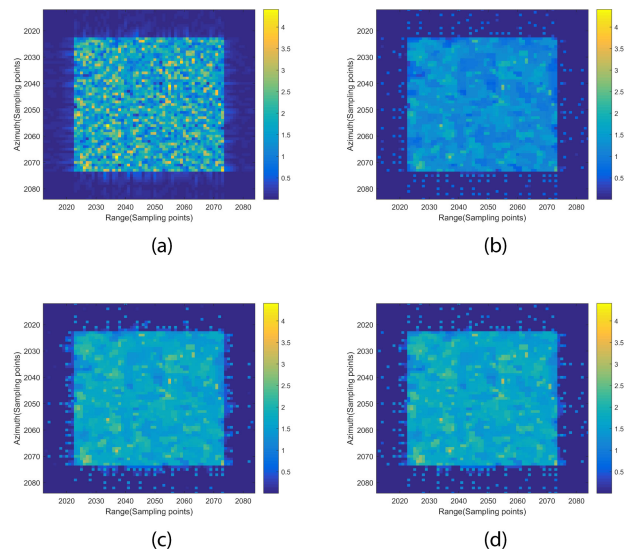
In the 2-D model, we place a distributed target that occupies 60×60 pixels at the center of the scene. In each pixel cell, there are normally many scatters whose amplitudes and phases are unobservable because the individual scatters are on much smaller scales than the resolution of the SAR. According to Oliver and Quegan [30], we set an equivalent phase center in each pixel cell, whose amplitudes are i.i.d. Rayleigh distributed $\mu = \sqrt{\pi \sigma_0}/2, \sigma^2 = \sqrt{(1 - \pi/4)\sigma_0}$ and phases are i.i.d. uniformly distributed $U(-\pi, +\pi)$. First, CSA is used to reconstruct the scene and the result is shown in Fig. 7(a) [31]. As analyzed above, the resulting complex image will be Rayleigh distributed in amplitude and uniformly distributed in phase, suffering from speckles. Then, we use the azimuth-range decouple operators-based ℓ_1 & TV regularization to reconstruct the scene. As shown in Fig. 7(b), the compound regularizer composed of the sparsity-inducing penalty and TV-norm penalty can maintain the continuity of the backscattering coefficient (σ_0) of distributed targets within a certain area. Finally, we use the azimuth-range decouple operators-based nonconvex & TV regularization proposed in this article to reconstruct the scene, with the result shown in

Fig. 8.　The experimental scene and selected point targets.

TABLE II
THE MEAN AND VARIANCE OF THE COMPLEX IMAGE AMPLITUDE

Algorithm	Mean μ	Variance σ^2
Chirp Scaling	1.7579	0.4968
ℓ_1+TV	1.2450	0.0973
MC+TV	1.7020	0.0974
SCAD+TV	1.7019	0.0975

Fig. 7(c) and (d). Based on the above results, we calculate the mean and variance of the complex image amplitude, with the numerical results listed in Table II. Comparing the statistical result, it is easy to find that ℓ_1 & TV regularization causes a large bias in pixel mean compared with the CSA. In contrast, nonconvex & TV regularization not only reduces the variance of the pixel amplitude, but also reduces the bias of the mean. Therefore, we can conclude that the azimuth-range decouple operators-based nonconvex & TV regularization method can improve the reconstruction accuracy as well as maintain the continuity of the backscattering coefficient (σ_0) of distributed targets within a certain area, which is of great significance for the estimation of the backscattering coefficient of distributed targets.

B. Real Data Processing

In order to show the influence of bias effect on practical application and validate the effectiveness of nonconvex penalty-based sparse SAR imaging algorithm in reducing the bias effect, we conduct the experiments using the data of Gaofen-3. Gaofen-3 is the first C-band multipolarization SAR in China; in this experiment, the stripmap mode data with HH polarization is used. The main parameters of this data are as follows: the bandwidth of the signal is 60 MHz, the sampling frequency in the range direction is 66.66 MHz, the Doppler bandwidth is 741.45 Hz, and the pulse repetition rate is 1149.45 Hz.

In the first part, we will analyze the reconstruction accuracy of the point target. We choose three strong scattering points in the red rectangle in Fig. 8 as the experimental objects. First, we reconstruct the experimental scene using CSA, ℓ_1 regularization, and nonconvex regularization separately under the full sampling condition. The reconstruction results are shown in Fig. 9, in
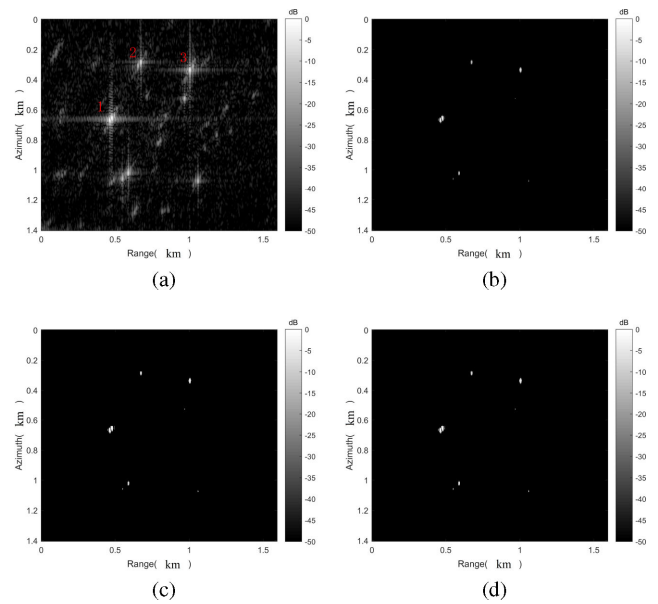

Fig. 9.　Reconstruction results of selected targets under the full sampling condition (normalized using the maximum amplitude in the result of chirp scaling algorithm under the full sampling condition). (a) Chirp Scaling. (b) ℓ_1. (c) MC. (d) SCAD.

which we can see that Fig. 9(b)–(d) has less noise and clutters compared with Fig. 9(a). Then we slice Target 1 labeled in Fig. 9(a) along the range direction in the result of chirp scaling, ℓ_1, MC, and SCAD. As shown in Fig. 10, ℓ_1 regularization does underestimate the amplitude of targets' complex reflectivity compared with the reconstruction result of CSA while nonconvex regularization can reconstruct the reflectivity of targets more accurately. In addition, we calculate the reflectivity of the three targets identified in Fig. 9(a) obtained by different reconstruction methods, and generate Table III. The statistical results listed in Table III can further verify the above conclusions.

Finally, we perform point target-experiments with undersampling ratio $= 60\%$ to observe the bias when the data is undersampled. Since there is no direct undersampling data, we simulate the undersampling process by randomly undersampling the full sampled data. Same as the full sampled data, we use chirp scaling algorithm, ℓ_1 regularization, and nonconvex regularization to
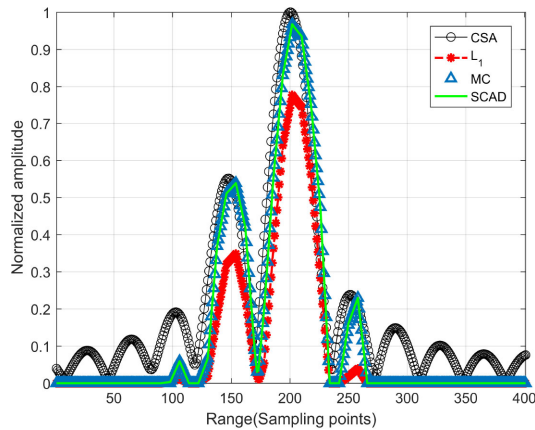
Fig. 10. Slices of Tar1 along the range direction in the result of Chirp Scaling, ℓ_1, MC, and SCAD (normalized using the maximum amplitude in the result of chirp scaling algorithm under the full sampling condition).

TABLE III
AMPLITUDE OF TARGETS UNDER THE FULL SAMPLING CONDITION FOR CHIRP SCALING ALGORITHM, ℓ_1 REGULARIZATION, AND NONCONVEX REGULARIZATION

Algorithm	Tar1	Tar2	Tar3
Chirp Scaling	3.5840	1.6332	2.5929
ℓ_1	2.8453	0.9349	1.8247
MC	3.5282	1.6179	2.5077
SCAD	3.5283	1.6179	2.5077

TABLE IV
AMPLITUDE OF TARGETS UNDER UNDERSAMPLING RATIO $= 60\%$ FOR CHIRP SCALING ALGORITHM, ℓ_1 REGULARIZATION, AND NONCONVEX REGULARIZATION

Algorithm	Tar1	Tar2	Tar3
Chirp Scaling	2.0555	0.94355	1.5086
ℓ_1	1.6347	0.55175	1.0731
MC	2.0171	0.93412	1.4554
SCAD	2.0171	0.93413	1.4554

reconstruct the target scene. As shown in Fig. 11(a), the reconstruction result of CSA will appear blurred phenomena along the azimuth direction when undersampling. In contrast, ℓ_1 regularization and nonconvex regularization can remove blurring and smearing in images. We also perform a slice analysis on Target 1 and calculate the reflectivity of the three targets, as shown in Fig. 12 and Table IV. According to the experimental results and statistical data, we can find that under the same sampling conditions, the reconstruction result of nonconvex regularization is more similar to that of CSA compared with ℓ_1 regularization.

In the second part, we will analyze the reconstruction accuracy and uniformity of the distributed target. Here, we select an approximately uniform island as the research object in the complete scene. The experimental scene is shown in Fig. 13, where the target island is identified by a red rectangular frame.

First, we use CSA to reconstruct the target scene. As shown in Fig. 14(a), there are many speckles in the image which cause the island to no longer be continuous and uniform. Then, we use
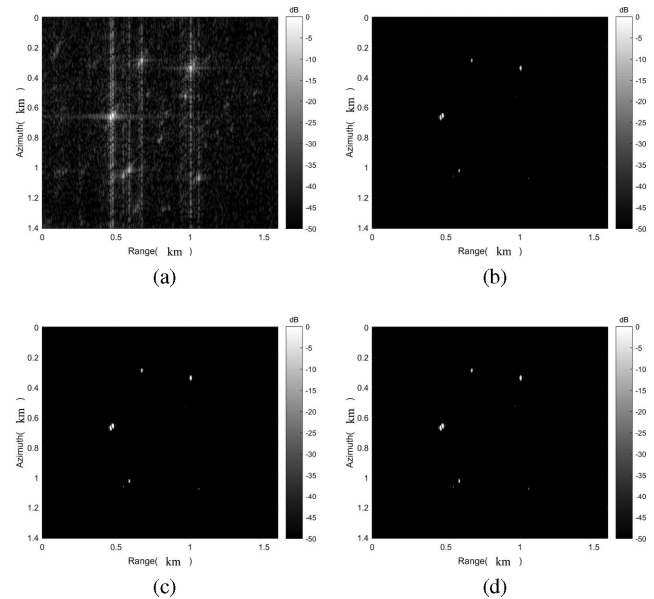

Fig. 11. Reconstruction results of selected targets with undersampling ratio $= 60\%$ (normalized using the maximum amplitude in the result of chirp scaling algorithm under undersampling ratio $= 60\%$). (a) Chirp scaling. (b) ℓ_1. (c) MC. (d) SCAD.
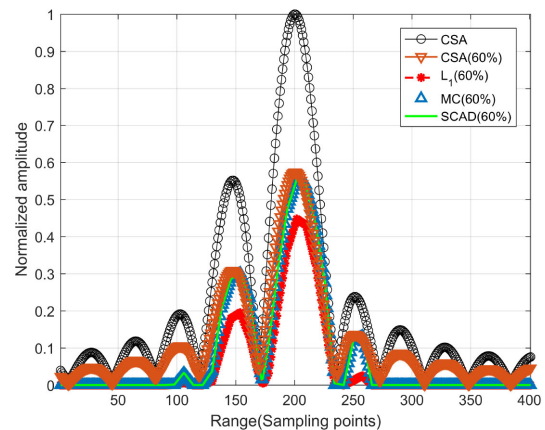

Fig. 12. Slices of Tar1 along the range direction in the result of chirp scaling, ℓ_1, MC, and SCAD with undersampling ratio $= 60\%$ (normalized using the maximum amplitude in the result of chirp scaling algorithm under the full sampling condition).

ℓ_1 & TV regularization to reconstruct the scene, and the result is shown in Fig. 14(b). Compared with Fig. 14(a), the results in Fig. 14(b) are significantly more uniform and continuous, and the clutters and noise in the image are also lower, which validates the effectiveness of the method. Since ℓ_1 regularization will bring bias effects, we also use nonconvex & TV regularization to reconstruct the scene, in which we select MC and SCAD as penalty functions, with the result shown in Fig. 14(c) and (d). For further quantitative analysis of bias and uniformity, we select three areas surrounded by the red rectangle on the island and calculate their mean and variance separately based on the above imaging results. The numerical results for areas 1, 2, and 3 correspond to Tables V–VII, respectively.

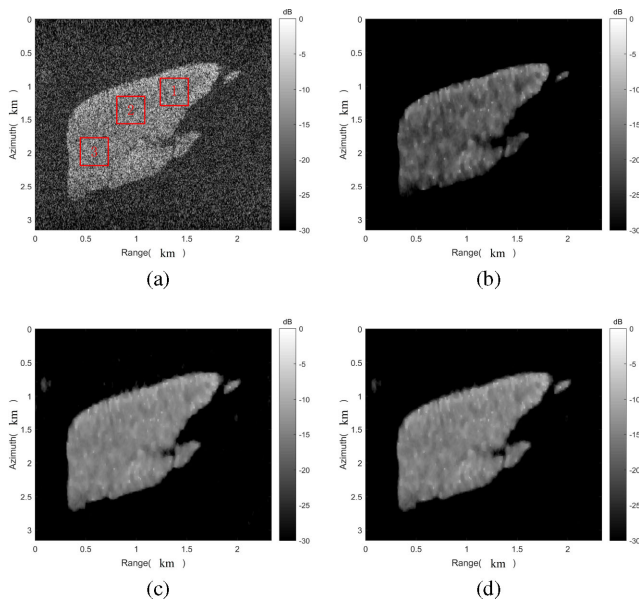Fig. 13.   The experimental scene and the target island.

Fig. 14.   Reconstruction results of the target island (normalized using the maximum amplitude in the result of chirp scaling algorithm). (a) Chirp scaling. (b) ℓ_1+TV. (c) MC+TV. (d) SCAD+TV.

TABLE V
THE MEAN AND VARIANCE OF AREA 1 SURROUNDED BY THE RED RECTANGLE ON THE ISLAND

Algorithm	Mean μ	Variance σ^2
Chirp Scaling	4.0001	4.9714
ℓ_1+TV	2.1480	0.2249
MC+TV	3.6857	0.2551
SCAD+TV	3.6100	0.2826

TABLE VI
THE MEAN AND VARIANCE OF AREA 2 SURROUNDED BY THE RED RECTANGLE ON THE ISLAND

Algorithm	Mean μ	Variance σ^2
Chirp Scaling	3.6965	3.9221
ℓ_1+TV	1.8755	0.1122
MC+TV	3.3993	0.1390
SCAD+TV	3.3106	0.1605

TABLE VII
THE MEAN AND VARIANCE OF AREA 3 SURROUNDED BY THE RED RECTANGLE ON THE ISLAND

Algorithm	Mean μ	Variance σ^2
Chirp Scaling	3.7910	4.1349
ℓ_1+TV	1.9481	0.1363
MC+TV	3.4861	0.1556
SCAD+TV	3.4031	0.1751

Based on the imaging results shown in Fig. 14 and the statistical results in Tables V–VII, we can find that compared with the traditional CSA, the nonconvex & TV regularization method proposed in this article can suppress noise and clutter, as well as reduce variance of reconstruction results to maintain the uniformity and continuity of the distributed target. More importantly, compared with the ℓ_1 & TV regularization, the mean value of the reconstruction results using this method is closer to the result of CSA, which shows that the method can effectively reduce bias and achieve higher reconstruction accuracy.

IV. DISCUSSION

A. Bias Effect Under Different Undersampling Ratios and SNRs

In order to study the variation of bias effect with undersampling ratios and SNRs, we repeat the 1-D simulation described in Section III-A under different conditions.
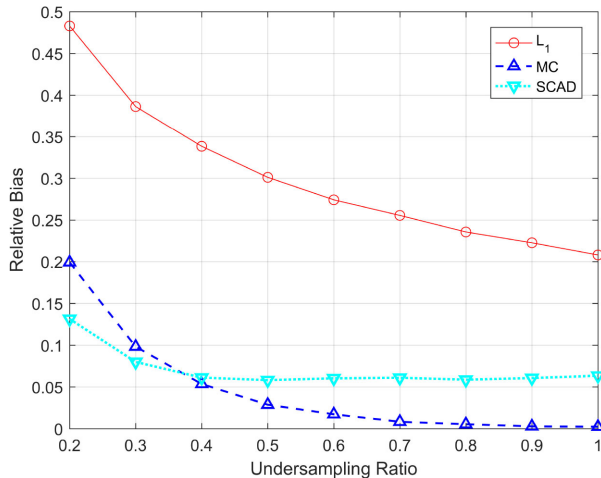
Fig. 15.   Relative bias under different undersampling ratios.

Fig. 16.   Relative bias of targets under different SNR conditions.

First, we perform experiments under different undersampling ratios to explore the effect of undersampling ratios on bias. In this experiment, the SNR is set to 20 dB, the range of under-sampling ratio is $[20\%, 100\%]$, and the interval is 10%. Under each undersampling ratio condition, we use the Monte–Carlo method to perform 500 repeated experiments, and generate the undersampling matrix randomly in each experiment. Finally, we average the experimental results to obtain the bias. From the experimental results shown in Fig. 15, we can find that a low undersampling ratio leads to an increase in bias. At the same time, we can observe that under the same experimental conditions, the bias of nonconvex regularization is much smaller than ℓ_1 regularization.

Then, experiments are carried out under different SNR conditions in order to study the influence of SNR on bias effect as well as test the adaptability of the proposed method in this article to different noise environments. This experiment is carried out under the full sampling condition, the variation range of SNR is $[10, 25]$ dB and the interval is 1 dB. Under each SNR condition, we use the Monte–Carlo method to perform 500 repeated experiments, and generate random noise in each experiment. Finally, we average the experimental results to obtain the bias. As shown in Fig. 16, the relative bias increases with the increasing of the noise level for all these three algorithms. However, under the same SNR condition, nonconvex regularization performs better than ℓ_1 regularization, which implies the method has a certain ability to adapt to the harsh noise environment.

B. Equivalent Number of Looks for Reconstruction Results

Equivalent number of looks (ENL) is commonly used to measure the speckle suppression of different SAR image filters [32]. When the ENL value is bigger, it indicates the image is smoothed well. The definition of ENL is as follows:

$$\text{ENL} = \frac{\mu(I)^2}{\sigma(I)^2} \tag{36}$$

where $I = Amplitude^2$ denotes the intensity of SAR image, $\mu(I)$ is the mean of I, and $\sigma(I)$ is the standard deviation of I.
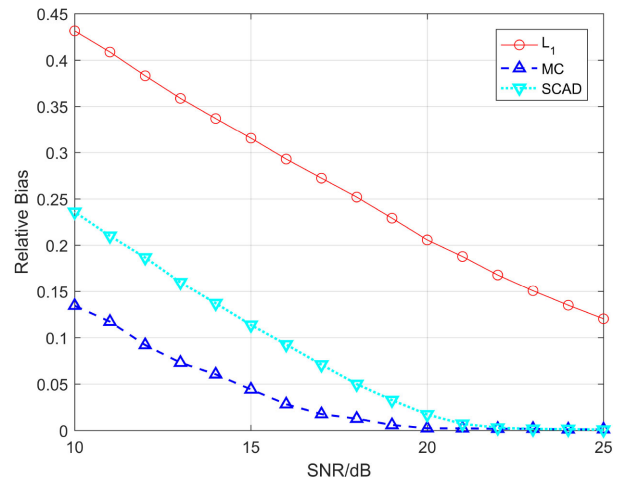
TABLE VIII
ENL FOR RECONSTRUCTION RESULTS

Algorithm	Area1	Area2	Area3
Chirp Scaling	0.9122	0.8790	0.8025
ℓ_1+TV	6.7979	5.8115	3.5750
MC+TV	19.4911	17.5498	10.7465
SCAD+TV	15.9309	14.8309	9.2008

As described in (36), ENL contains both mean and variance of the image, so it is more reasonable to measure the continuity of the reconstruction results with ENL.

As in the second part of Section III-B, we calculate ENL of the target island in Fig. 14, with the results shown in Table VIII. The data in this article has not been multilook processed, so the ENL of the reconstruction results based on the traditional CSA are approximately equal to 1. In contrast, ℓ_1 & TV regularization and nonconvex & TV regularization can effectively improve the ENL. Meanwhile, due to the bias effect of ℓ_1 regularization, the $\mu(I)$ of reconstruction results based on nonconvex & TV regularization is larger than that of ℓ_1 & TV regularization, for which the proposed method in this article can increase the ENL more effectively. Therefore, nonconvex & TV regularization can maintain the continuity of targets while improving the reconstruction accuracy.

V. CONCLUSION

The analytic solution of ℓ_1 regularization-based sparse signal reconstruction algorithm is a biased estimation, which leads to the underestimation of targets' reflectivity when applied to sparse SAR imaging. In order to reduce the bias effect and improve the reconstruction accuracy, we adopt the nonconvex regularization-based sparse SAR imaging method with nonconvex penalty family. In this article, we quantitatively analyze the variation of reconstruction bias with respect to complex reflectivity of targets, undersampling ratio, and noise power. After simulations and experiments with real data, we get the following conclusions. First, the relative bias of targets becomes larger

as the amplitude of reflectivity decreases for ℓ_1 regularization, which means that the bias effect has a greater impact on weak targets. In contrast, nonconvex regularization can control the relative bias at a low level. Second, a low undersampling ratio leads to an increase in bias. At the same time, we can observe that under the same experimental conditions, the bias of nonconvex regularization is much smaller than ℓ_1 regularization. Finally, the relative bias increases with the increase of the noise level for ℓ_1 regularization as well as nonconvex regularization. However, under the same SNR condition, nonconvex regularization performs better than ℓ_1 regularization, which implies the method has a certain ability to adapt to the harsh noise environment.

In order to enhance point-based features as well as region-based features, this article linearly combines the nonconvex penalty and the TV-norm penalty as a compound regularizer in the imaging model, which can improve the reconstruction accuracy of distributed targets as well as maintain the continuity of the backscattering coefficient in uniform regions. In large-scale SAR imaging, storage and processing of measurement matrix would bring huge memory and computational cost. Therefore, we adopt the azimuth-range decouple scheme in the real data processing. Experiments based on real data from Gaofen-3 satellites verify that the nonconvex & TV regularization method proposed in this article can suppress noise and clutter, as well as reduce variance of reconstruction results to maintain the uniformity and continuity of the distributed target, which implies the huge potential and advantages of the proposed method in RCS estimation, target classification, and image segmentation.

REFERENCES

[1] B. Zhang, W. Hong, and Y. Wu, "Sparse microwave imaging: Principles and applications," *Sci. China Inf. Sci.*, vol. 55, no. 8, pp. 1722–1754, 2012.

[2] J. H. Ender, "On compressive sensing applied to radar," *Signal Process.*, vol. 90, no. 5, pp. 1402–1414, 2010.

[3] M. Cetin *et al.*, "Sparsity-driven synthetic aperture radar imaging: Reconstruction, autofocusing, moving targets, and compressed sensing," *IEEE Signal Process. Mag.*, vol. 31, no. 4, pp. 27–40, Jul. 2014.

[4] J. Fang, Z. Xu, B. Zhang, W. Hong, and Y. Wu, "Fast compressed sensing SAR imaging based on approximated observation," *IEEE J. Sel. Top. Appl. Earth Observ. Remote Sens.*, vol. 7, no. 1, pp. 352–363, Jan. 2014.

[5] H. Bi, B. Zhang, X. X. Zhu, C. Jiang, and W. Hong, "Extended chirp scaling-baseband azimuth scaling-based azimuth–range decouple ℓ_1 regularization for tops SAR imaging via camp," *IEEE Trans. Geosci. Remote Sens.*, vol. 55, no. 7, pp. 3748–3763, Jul. 2017.

[6] X. Quan, B. Zhang, X. X. Zhu, and Y. Wu, "Unambiguous SAR imaging for nonuniform DPC sampling: l_q regularization method using filter bank," *IEEE Geosci. Remote Sens. Lett.*, vol. 13, no. 11, pp. 1596–1600, 2016.

[7] S. Boyd *et al.*, "Distributed optimization and statistical learning via the alternating direction method of multipliers," *Foundations Trends Mach. learn.*, vol. 3, no. 1, pp. 1–122, 2011.

[8] M. Elad, *Sparse and Redundant Representations: From Theory to Applications in Signal and Image Processing*. New York, NY, USA: Springer Science & Business Media, 2010.

[9] A. Chambolle, "An algorithm for total variation minimization and applications," *J. Math. Imag. Vis.*, vol. 20, no. 1–2, pp. 89–97, 2004.

[10] A. Chambolle *et al.*, "Total variation minimization and a class of binary MRF models," in *International Workshop Energy Minimization Methods Comput. Vision Pattern Recognit*, Springer, 2005, pp. 136–152.

[11] M. Çetin and W. C. Karl, "Feature-enhanced synthetic aperture radar image formation based on nonquadratic regularization," *IEEE Trans. Image Process.*, vol. 10, no. 4, pp. 623–631, Apr. 2001.

[12] H. E. Güven, A. Güngör, and M. Cetin, "An augmented lagrangian method for complex-valued compressed SAR imaging," *IEEE Trans. Comput. Imag.*, vol. 2, no. 3, pp. 235–250, Sep. 2016.

[13] Y. Zhao, J. G. Liu, B. Zhang, W. Hong, and Y.-R. Wu, "Adaptive total variation regularization based SAR image despeckling and despeckling evaluation index," *IEEE Trans. Geosci. Remote Sens.*, vol. 53, no. 5, pp. 2765–2774, May 2015.

[14] E. Candes *et al.*, "The Dantzig selector: Statistical estimation when p is much larger than n," *Ann. Statist.*, vol. 35, no. 6, pp. 2313–2351, 2007.

[15] S. Osher, F. Ruan, J. Xiong, Y. Yao, and W. Yin, "Sparse recovery via differential inclusions," *Appl. Comput. Harmon. Anal.*, vol. 41, no. 2, pp. 436–469, 2016.

[16] Z. Xu, Z. Wei, M. Liu, B. Zhang, and Y. Wu, "Analysis and suppression of bias effect in sparse SAR imaging," in *Image and Signal Processing for Remote Sensing*. Strasbourg, France: International Society for Optics and Photonics, 2019, p. 111551E.

[17] Z. Wei, B. Zhang, Z. Xu, B. Han, W. Hong, and Y. Wu, "An improved SAR imaging method based on nonconvex regularization and convex optimization," *IEEE Geosci. Remote Sens. Lett.*, vol. 16, no. 10, pp. 1580–1584, Oct. 2019.

[18] C.-H. Zhang *et al.*, "Nearly unbiased variable selection under minimax concave penalty," *Ann. Statist.*, vol. 38, no. 2, pp. 894–942, 2010.

[19] I. Selesnick, "Sparse regularization via convex analysis," *IEEE Trans. Signal Process.*, vol. 65, no. 17, pp. 4481–4494, Sep. 2017.

[20] J. Fan and R. Li, "Variable selection via nonconcave penalized likelihood and its oracle properties," *J. Amer. Statistical. Assoc.*, vol. 96, no. 456, pp. 1348–1360, 2001.

[21] F. Wen, L. Chu, P. Liu, and R. C. Qiu, "A survey on nonconvex regularization-based sparse and low-rank recovery in signal processing, statistics, and machine learning," *IEEE Access*, vol. 6, pp. 69883–69906, 2018.

[22] G. Gasso, A. Rakotomamonjy, and S. Canu, "Recovering sparse signals with a certain family of nonconvex penalties and DC programming," *IEEE Trans. Signal Process.*, vol. 57, no. 12, pp. 4686–4698, Dec. 2009.

[23] P. Gong, C. Zhang, Z. Lu, J. Huang, and J. Ye, "A general iterative shrinkage and thresholding algorithm for non-convex regularized optimization problems," in *Proc. Int. Conf. Mach. Learn.*, 2013, pp. 37–45.

[24] J. M. Bioucas-Dias and M. A. Figueiredo, "An iterative algorithm for linear inverse problems with compound regularizers," in *Proc. 15th IEEE Int. Conf. Image Process.*, 2008, pp. 685–688.

[25] E. J. Candes, "The restricted isometry property and its implications for compressed sensing," *Comptes Rendus Mathematique*, vol. 346, pp. 589–592, 2008.

[26] Z. Wei, B. Zhang, B. Han, Z. Xu, W. Hong, and Y. Wu, "An accurate SAR imaging method based on generalized minimax concave penalty," in *Proc. 12th Eur. Conf. Synthetic Aperture Radar*, VDE, 2018, pp. 1–6.

[27] D. Tuia, R. Flamary, and M. Barlaud, "Nonconvex regularization in remote sensing," *IEEE Trans. Geosci. Remote Sens.*, vol. 54, no. 11, pp. 6470–6480, Nov. 2016.

[28] M. V. Afonso, J. M. Bioucas-Dias, and M. A. Figueiredo, "Fast image recovery using variable splitting and constrained optimization," *IEEE Trans. Image Process.*, vol. 1, no. 9, pp. 2345–2356, Sep. 2010.

[29] M. V. Afonso, J. M. Bioucasdias, and M. A. T. Figueiredo, "An augmented lagrangian approach to the constrained optimization formulation of imaging inverse problems," *IEEE Trans. Image Process.*, vol. 20, no. 3, pp. 681–695, Mar. 2011.

[30] C. Oliver and S. Quegan, *Understanding Synthetic Aperture Radar Images*. Raleigh, NC, USA: SciTech Publishing, 2004.

[31] R. K. Raney, H. Runge, R. Bamler, I. G. Cumming, and F. H. Wong, "Precision SAR processing using chirp scaling," *IEEE Trans. Geosci. Remote Sens.*, vol. 32, no. 4, pp. 786–799, Jul. 1994.

[32] A. Freeman, "SAR calibration: An overview," *IEEE Trans. Geosci. Remote Sens.*, vol. 30, no. 6, pp. 1107–1121, Nov. 1992.

Zhongqiu Xu received the bachelor's degree from the Beijing Institute of Technology, Beijing, China, in 2018. He is currently working toward the Ph.D. degree in signal and information processing at the University of Chinese Academy of Sciences, Beijing, China.

His research interests include radar signal processing, compressed sensing, and sparse SAR imaging.

Mingqian Liu received the bachelor's degree from the Beijing Institute of Technology, Beijing, China, in 2017. He is currently working toward the Ph.D. degree in signal and information processing at the University of Chinese Academy of Sciences, Beijing, China.

His research interests include radar signal processing, compressed sensing, and sparse SAR imaging.

Guoru Zhou received the bachelor's degree from the Beijing Institute of Technology, Beijing, China, in 2020. She is currently working toward the Ph.D. degree in signal and information processing with the University of Chinese Academy of Sciences, Beijing, China.

Her research interests include radar signal processing, compressed sensing, and sparse SAR imaging.

Zhonghao Wei received the B.S. degree in electronic engineering and information science from the University of Electronic Science and Technology of China, Chengdu, China, in 2014, and the Ph.D. degree from the University of Chinese Academy of Sciences, Beijing, China, in 2019.

He is currently with the Nanjing Research Institute of Electronics Technology, Nanjing, China. His research interest includes the areas of SAR imaging.

Bingchen Zhang received the bachelor's degree from the University of Science and Technology of China, Hefei, China, in 1996 and the M.S. degree from the Institute of Electronics, Chinese Academy of Sciences (IECAS), Beijing, China, in 1999.

Since 1999, he has been a Scientist with IECAS. His research interests include synthetic aperture radar (SAR) signal processing and airborne SAR system design, implementation, and data processing.

Yirong Wu received the Ms.D. degree from the Beijing Institute of Technology, Beijing, China, in 1988 and the Ph.D. degree from the Institute of Electronics, Chinese Academy of Sciences (IECAS), Beijing, China, in 2001.

Since 1988, he has been with IECAS, where he currently serves as the Director. He has over 20 years of experience in remote-sensing processing system design. His research interests include microwave imaging, signal and information processing, and related applications.